

## Tin induced $\alpha$ -Si crystallization in thin films of Si-Sn alloys

V. Neimash, V. Poroshin, P. Shepeliavyi, V. Yukhymchuk, V. Melnyk, A. Kuzmich, V. Makara, and A. O. Goushcha

Citation: *Journal of Applied Physics* **114**, 213104 (2013); doi: 10.1063/1.4837661

View online: <http://dx.doi.org/10.1063/1.4837661>

View Table of Contents: <http://scitation.aip.org/content/aip/journal/jap/114/21?ver=pdfcov>

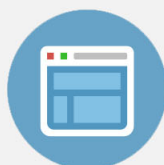
Published by the [AIP Publishing](#)

---

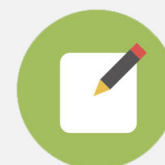


## Re-register for Table of Content Alerts

Create a profile.



Sign up today!



# Tin induced $\alpha$ -Si crystallization in thin films of Si-Sn alloys

V. Neimash,<sup>1,a)</sup> V. Poroshin,<sup>1</sup> P. Shepeliavyi,<sup>2</sup> V. Yukhymchuk,<sup>2</sup> V. Melnyk,<sup>3</sup> A. Kuzmich,<sup>3</sup> V. Makara,<sup>3</sup> and A. O. Goushcha<sup>1,a),b)</sup>

<sup>1</sup>*Institute of Physics, National Academy of Sciences of Ukraine, 46 Nauky Ave., 03028 Kyiv, Ukraine*

<sup>2</sup>*Institute of Semiconductor Physics, National Academy of Sciences of Ukraine, 45 Nauky Ave., 03028 Kyiv, Ukraine*

<sup>3</sup>*Faculty of Physics, Taras Shevchenko National University of Kyiv, 60 Volodymyrska St., 01601 Kyiv, Ukraine*

(Received 15 October 2013; accepted 14 November 2013; published online 6 December 2013)

Effects of tin doping on crystallization of amorphous silicon were studied using Raman scattering, Auger spectroscopy, scanning electron microscopy, and X-ray fluorescence techniques. Formation of silicon nanocrystals (2–4 nm in size) in the amorphous matrix of  $\text{Si}_{1-x}\text{Sn}_x$ , obtained by physical vapor deposition of the components in vacuum, was observed at temperatures around 300 °C. The aggregate volume of nanocrystals in the deposited film of  $\text{Si}_{1-x}\text{Sn}_x$  exceeded 60% of the total film volume and correlated well with the tin content. Formation of structures with  $\sim 80\%$  partial volume of the nanocrystalline phase was also demonstrated. Tin-induced crystallization of amorphous silicon occurred only around the clusters of metallic tin, which suggested the crystallization mechanism involving an interfacial molten Si:Sn layer. © 2013 AIP Publishing LLC.  
[\[http://dx.doi.org/10.1063/1.4837661\]](http://dx.doi.org/10.1063/1.4837661)

## I. INTRODUCTION

Nanocrystalline silicon (Si) thin films are one of the most promising materials for photovoltaic solar energy conversion.<sup>1</sup> A controlled crystallization of amorphous silicon films from the amorphous state was studied intensively during the past decades. Recently, those studies gained an additional momentum due to advances with metal-assisted transformation of amorphous Si ( $\alpha$ -Si) into a crystalline state.<sup>2–5</sup> Silicon doping with tin (Sn) proved to be an effective and convenient method of influencing various properties of Si. As the isovalent dopant, Sn does not create energy levels in the band gap of Si. Therefore, doping with Sn within its solubility level does not affect electrical, optical, and recombination properties of crystalline Si. At the same time, the presence of Sn atoms inhibits effectively the performance degradation of crystalline Si under various harmful conditions such as heat treatment<sup>6–8</sup> and ionizing radiation.<sup>8–11</sup> In amorphous Si, doping with Sn significantly reduces the optical bandgap ( $E_g$ )<sup>12–14</sup> and changes some other physical characteristics of the material. In particular, it was shown that at low concentrations of Sn, the electrical conductivity of Si:Sn alloy is characterized with a reduced activation energy of about  $E_g/2$ .<sup>14,15</sup> Moreover, with increasing Sn concentration in the range from 1 to 2 at. %, the hopping conductivity mechanism prevails. Light absorption in thin film alloys  $\text{Si}_{1-x}\text{Sn}_x$  occurs via the direct band gap transition mechanism.<sup>15</sup> However, when adding the other isovalent impurity, carbon (C) to this alloy, a reverse to indirect band gap transitions may occur.<sup>16</sup>

Despite of a significant number of works studying Si:Sn alloys, the effects of Sn-assisted crystallization of amorphous

Si were not characterized comprehensively. Tin atoms in  $\alpha$ -Si can substitute the host atoms either in the tetragonal<sup>17</sup> or non-tetragonal<sup>16</sup> configuration forming either a regular or non-regular grid. Under certain conditions, the precipitates of Sn atoms are formed in the amorphous matrix of Si.<sup>15,18</sup> Tin is one of the eutectic forming metals<sup>19</sup> that may induce a transition of amorphous Si into the crystalline state due to layer exchange effects on the metal-silicon interface.<sup>2,20</sup> Such metal induced crystallization (MIC) was observed at a relatively low-temperature (300–500 °C) anneal of sandwiches of thin films of amorphous Si and metallic Sn deposited on a glass substrate.<sup>2,21</sup> Raman spectroscopy (RS) results demonstrated the ability of Sn impurities to accelerate significantly crystallization of  $\alpha$ -Si when growing thin films of  $\text{Si}_{1-x}\text{Sn}_x$  by thermal evaporation of the components in vacuum.<sup>22</sup> However, within a thin surface layer of  $\sim 25$  nm thickness, the Sn concentration was 5–6 times higher than in the bulk of the film.<sup>23</sup> The laser radiation in the green spectral range used for Raman excitation<sup>22</sup> was completely absorbed within the 30–35 nm thickness surface layer of the direct band-gap (amorphous) silicon, introducing uncertainties to the analysis of the mechanisms of Sn effect on crystallization of  $\alpha$ -Si. Creating a precisely controlled, uniform concentration of Sn within the surface layer accessible to Raman excitation is imperative for a reliable analysis of the experimental results. The goal of this work was to investigate conditions of forming a uniform polycrystalline Si films during crystallization of a binary alloy Si-Sn at tightly controlled Sn concentration and to characterize the crystalline vs amorphous phase formation at different concentrations of Sn.

## II. EXPERIMENT

Si:Sn alloy films with the thickness of 300–500 nm were prepared by thermal evaporation in vacuum of the powder mixtures of high-purity Si and Sn. Sn content in the mixtures varied from 0.1 to 30 wt. %. Quartz and mono-crystalline Si

<sup>a)</sup>Authors to whom correspondence should be addressed. Electronic addresses: neimash@iop.kiev.ua and oleks.goushcha@nuportsoft.com.

<sup>b)</sup>Present address: NuPortSoft, 21 Nopalitos Way, Aliso Viejo, California 92656, USA.

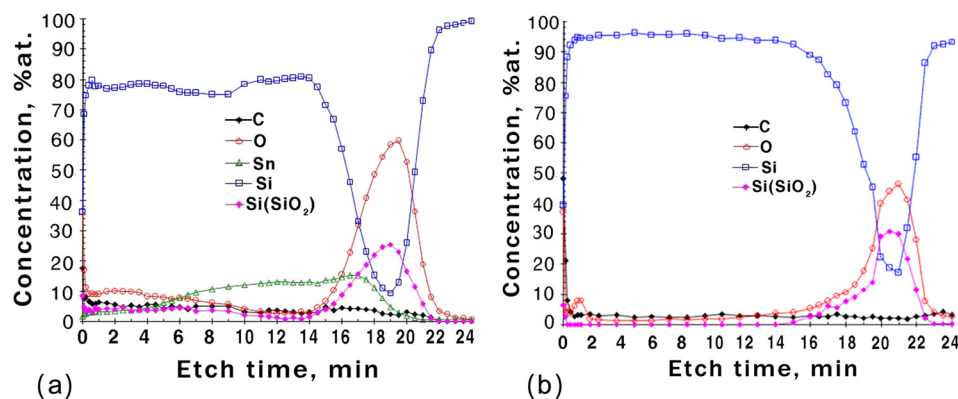


FIG. 1. Typical concentration profiles in grown films: (a) Si:Sn film containing 2.5 at. % of Sn; (b) control film of amorphous Si grown with no Sn dopant. The etch rate was 20 nm/min.

wafers were used as substrates to form Si:Sn films at a temperature of 300 °C and a residual pressure of  $10^{-3}$  Pa. The deposition parameters were tightly controlled to ensure a uniform distribution of Sn in  $\sim 100$  nm thickness surface layer of the film.<sup>23</sup> The total thickness of the deposited Si:Sn films varied from 250 to 800 nm. No additional anneal was applied. The amorphous vs crystalline phase composition of the films was analyzed using room temperature. RS activated with Ar-Kr<sup>+</sup>-laser at the wavelength of 514.5 nm. The impurity distribution profiles across the films were characterized by Auger electron spectroscopy of reactive ion etched (RIE) films. Scanning electron microscopy (SEM) and X-ray fluorescence micro-probing (energy dispersive X-ray spectroscopy, EDX) were used for studying the surface topology and impurities distribution on the surface.

### III. RESULTS

Figure 1 shows typical concentration profiles in the alloy film Si:Sn (a) and amorphous silicon control sample without Sn (b) as measured by Auger electron spectroscopy of reactive ion etched films. The films were grown on crystalline silicon substrates with the thermal oxide thickness of  $\sim 100$  nm. The total thickness of deposited films described in Figure 1 was  $\sim 300$  nm.

The details of Sn concentration profile as well as the concentration profile features for the technological impurities carbon and oxygen (O), within the surface layer accessible for Raman excitation with 514.5 nm light, are shown in Figure 2. The distribution of technological impurities C and O was similar in both samples. The measured Sn concentration profile showed good uniformity within  $\sim 40$  nm of the

surface layer. The same good uniformity of Sn concentration was measured for the films with different content of Sn, which allowed a straightforward and reliable analysis of Raman spectroscopy data.

The phase structure of the samples with various Sn content was analyzed using Raman spectroscopy data. Figure 3 shows changes in Raman spectra of Si:Sn alloys with increasing Sn content. The spectra were recorded using a large diameter laser beam (3 mm) to measure the spectra integrated over a large surface. Care was taken to provide a uniform excitation across the 3 mm spot of the sample surface. A broad band at around  $470\text{ cm}^{-1}$  corresponds to amorphous silicon. A narrow band centered around  $515\text{ cm}^{-1}$  corresponds to Si in the crystalline state. The amplitude of this narrow band is defined by the portion of the material in the crystalline phase, whereas the peak's frequency position is defined by the dominant size of the crystallites.<sup>24–26</sup> The characteristic band at around  $515\text{ cm}^{-1}$  emerged in the samples having Sn content of 2.5 at. %. With increasing Sn concentration beyond 2.5 at. %, the amplitude of this band increased significantly, but the frequency of its peak shifted only slightly to higher frequencies. The above observations indicated that a higher Sn content stimulated crystallization of amorphous Si by increasing the number of (nano)-crystals without significant changes in their dominant size.

The partial volume of the crystalline phase in the film was estimated using the expression<sup>25</sup>

$$X_c = (I_c/I_a)/(y + I_c/I_a), \quad (1)$$

where  $I_c$  and  $I_a$  are the integrated intensities of the crystalline and amorphous components in Raman spectra, respectively.

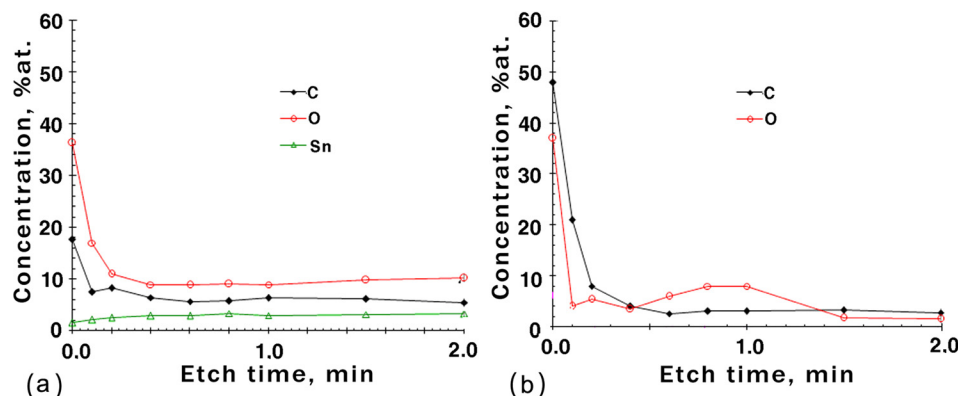


FIG. 2. Details of the concentration profiles in the surface layers of the grown films: (a) Si:Sn film containing 2.5 at. % of Sn; (b) control film of amorphous Si grown with no Sn dopant. The etch rate was 20 nm/min.

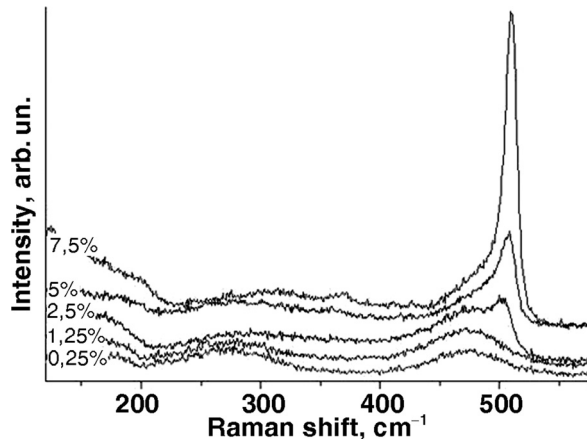


FIG. 3. Raman spectra of Si:Sn alloys with Sn content within the range 0.25–7.5 at. %. The laser beam diameter was  $\sim 3$  mm.

The ratio  $y$  of the scattering cross sections of the crystalline and amorphous Si was determined using<sup>24</sup>

$$y(L) = 0.1 + \exp(-L/25), \quad (2)$$

in which  $L$  is an average size of nano-crystals (in nanometers) that can be estimated using the expression for the scattering intensity  $I$  at frequency  $\nu$ <sup>25</sup>

$$I(\nu) = \int \exp[-(q^2 L^2)/(16\pi^2)] / [(\nu - \nu(q))^2 + (\Gamma_0/2)^2] d^3 q, \quad (3)$$

where  $\Gamma_0$  is the half-width of the Raman band of a crystalline Si;  $\nu(q)$  is the dispersion relation for the phonon vibrations in crystalline Si.

The intensity of Raman scattering originating from the  $\alpha$ -Si phase is well described by the Gaussian distribution,<sup>24</sup>

$I(\nu) = B \exp[-(\nu - \nu_a)^2/(2\delta^2)]$ , where  $B$  is a constant,  $\delta = \Gamma_a/(2\sqrt{2\ln 2})$ , and  $\nu_a$  and  $\Gamma_a$  are the frequency of the maximum of the  $\alpha$ -Si scattering band and its full width at half-maximum, respectively.

Deconvolution of Raman spectra of Figure 3 in the range from 400 to 540  $\text{cm}^{-1}$  into Gaussian and asymmetric (Eq. (3)) components allowed estimating the partial volumes of the two phases in the thin films. We used the Levenberg-Marquardt nonlinear least square deconvolution algorithm to analyze Raman spectra of Figure 3. In all cases, best fitting results were obtained using two components. Adding more asymmetric or Gaussian components caused deconvolution to converge with negligible weights of additional components, proving rather uniform distribution of nanocrystal sizes.

Figure 4 shows deconvolution results for Si:Sn alloys containing 2.5, 5.0, and 7.5 at. % of Sn. Table I summarizes the calculation results using Eqs. (1)–(3).

Above results indicated that doping with Sn stimulated formation of the crystalline phase in Si:Sn alloy at the Sn content starting around 1.25–2.5 at. %. This finding was in good agreement with the early results on Sn concentration dependence of the hopping conductivity mechanism onset in Si:Sn alloys.<sup>14,15</sup> A further increase of the Sn content from 2.5 to 7.5 at. % caused an increase of the crystalline phase partial volume from 25% to 61% with only minor change in the dominant size of nanocrystals, from  $\sim 2.3$  nm to  $\sim 3.0$  nm.

The quasi-spherical droplets surrounded with the dendrite-like aureoles were observed on the surface of the films with the Sn content of 2.5 at. % and higher. The size and density distribution of these features correlated well with the Sn content of the films. Figure 5 shows representative SEM images of the film containing 5.0 at. % of Sn.

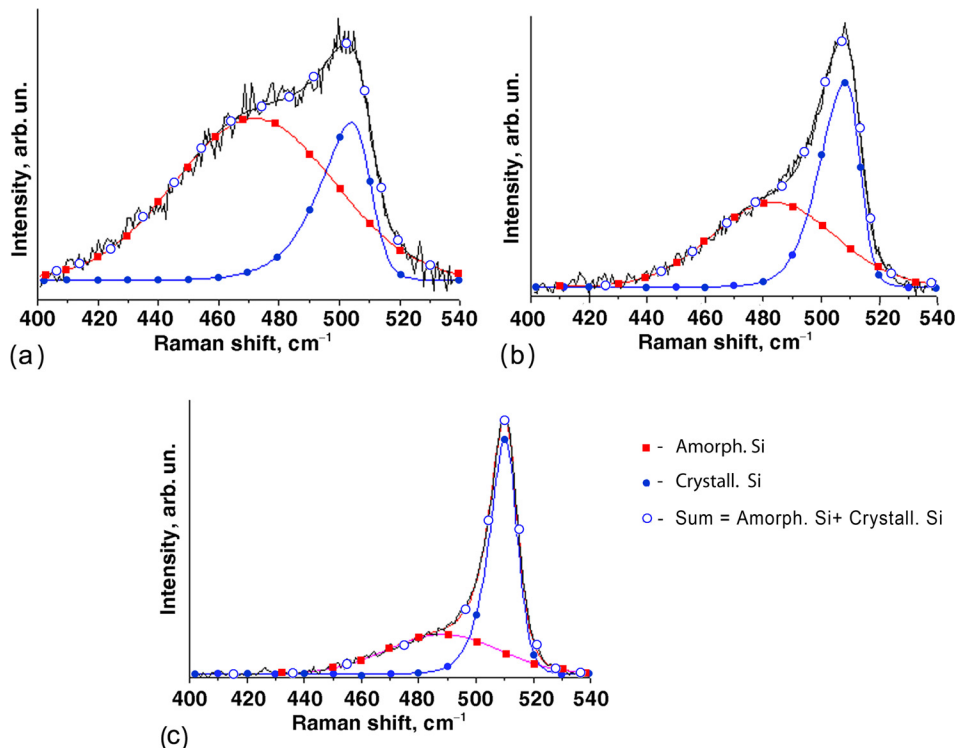


FIG. 4. Raman spectra deconvolution into the Gaussian (amorphous, line with solid squares) and asymmetric (crystalline, line with solid circle) components for the films with Sn content (a) 2.5 at. %, (b) 5.0 at. %, (c) 7.5 at. %. Line with open circles is the sum of two components shown with solid circles and squares.



TABLE I. The crystal average (dominant) size  $L$  and crystalline phase partial volume  $X_c$  for the samples containing 2.5, 5.0, and 7.5 at. % of Sn.

Sn content (at. %)	$I_c$	$I_a$	$I_c/I_a$	$L$	$X_c$
2.5	25.7	75.7	0.34	$2.3 \pm 0.1$	$0.25 \pm 0.02$
5.0	45.6	54.4	0.84	$2.7 \pm 0.1$	$0.46 \pm 0.015$
7.5	61.0	39.1	1.56	$3.0 \pm 0.15$	$0.61 \pm 0.01$

The EDX micro-probing of six different sites outlined with the squares in the panel (b) of Figure 5 confirmed that a quasi-spherical formation in the middle of the image of panel (b) is a droplet of metallic Sn covered with a thin oxidation layer (see Table II for a summary). The aureoles around the droplets (light grey areas in the images of Figure 5) contained Sn in the concentration twice of that outside the aureoles (dark grey areas in the images of Figure 5).

To determine the phase composition (crystalline vs. amorphous Si) of the film around Sn droplets, confocal Raman micro spectroscopy was used with the microprobe delivering excitation light to  $1\ \mu\text{m}$  diameter spot. Figure 6(a) shows the optical image of the same sample as in Figure 5. A bright yellow spot in the center of the image is a Sn droplet. The droplet is surrounded by a dark aureole, which is the same material that shows up with light grey aureoles in the SEM images of Figure 5.

The Raman spectra were taken at different distances from the Sn droplet boundary—both within the aureole area (site 1 in the image of Figure 6(a)) and outside the aureole (site 3 in Figure 6(a)). Site 2 in Figure 6(a) was located within a transition area separating the aureole and outside material.

The Raman spectra (Figure 6(b)) taken at different sites were markedly different from each other. The characteristic crystalline band around  $500\text{--}525\text{ cm}^{-1}$  was barely seen in

TABLE II. Results of EDX analysis at different probing sites of the sample shown in Figure 5(b). All data are in at. % units.

Probing site	C	O	Si	Sn
1	3.57	15.59	76.79	4.06
2	3.99	14.75	77.00	4.25
3	3.21	10.80	78.24	7.74
4	3.35	9.56	78.77	8.32
5	4.95	51.45	8.96	34.65
6	5.58	49.62	7.54	37.27

the spectrum from the site 3 and increased in intensity, while laser excitation approached the boundary of the Sn droplet. This band became dominant showing a sharp peak at  $\sim 525\text{ cm}^{-1}$  for the spectrum from the site 1. Table III presents the deconvolution results of the spectra from Figure 6(b) into Gaussian and asymmetric (Eq. (3)) components as described above, using the nonlinear least square deconvolution algorithm.

The partial volume of the crystalline phase of Si:Sn alloy was  $\sim 80\%$  for the probing site 1, close to the metallic Sn droplet. The partial volume of this phase dropped down to  $\sim 28\%$  outside the aureole surrounding the droplet (site 3). The dominant size of nanocrystals was largest close to the Sn droplet decreasing with the distance from the droplet. At the periphery of the aureole structure, the nanocrystals' size was close to that measured in the experiment with a 3 mm excitation spot (see results in Table I).

For the samples with Sn content lower than 2.5 at. %, we did not observe formation of metallic Sn droplets on the sample surface. No signature of the crystalline Si phase was observed in Raman spectra of these samples. Crystallization of Si occurred only in the samples where the metallic Sn droplets were formed.

#### IV. DISCUSSION

Analyzing metallic Sn droplets of different sizes, as well as the phase composition inside and outside the aureoles surrounding the droplets, we concluded that crystallization of Si starts at the metallic Sn droplet boundary and propagates outside the droplet. This finding agrees with recent reports<sup>2,21</sup> showing that annealing of thin planar structures of amorphous Si—metallic Sn at temperatures of  $300\text{--}500^\circ\text{C}$  leads to crystallization of Si within the eutectic layer close to the Si-Sn boundary. Formation of polycrystalline silicon films in the bi-layered structure of  $\alpha$ -Si film deposited on top of the metal film was discussed also in terms of the “layer exchange” process.<sup>20</sup> During the isothermal annealing of the structure, a continuous polycrystalline silicon film was formed within the initial metal layer and displaced it completely. Based on experimental observations, the authors concluded that Si atoms diffuse from the  $\alpha$ -Si film into the metal film forming the eutectic layer, where the nucleation of Si nanocrystals occurs. Electron screening at the interface with metals weakens Si covalent bonds, facilitating interdiffusion of metal atoms and silicon,<sup>27</sup> which triggers formation of a eutectic layer. Due to supply of Si atoms from the amorphous phase and fast diffusion constant of Si,

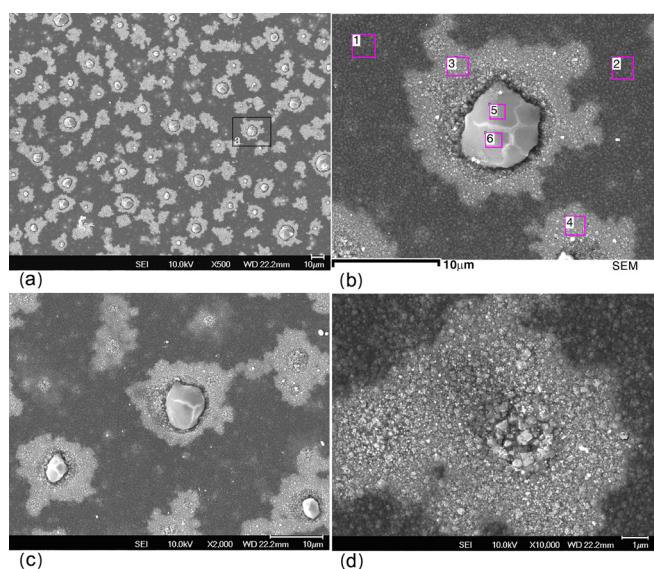


FIG. 5. SEM images of Si:Sn film with 5.0 at. % of Sn. Panel (a) is a low-resolution image of the film. Panel (b) shows the blow-up of the rectangular-outlined region “a” of panel (a). Panel (c) is a higher resolution image of several dendrites. Panel (d) shows a dendrite structure with a fully dissolved droplet (see the text below).

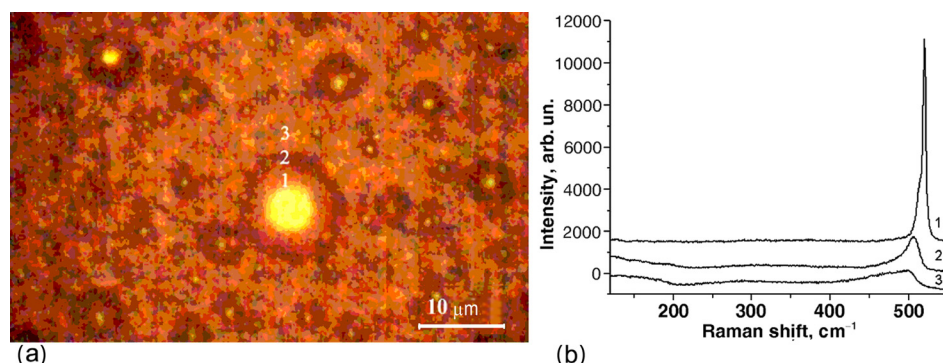


FIG. 6. (a) Image of the film taken with an optical microscope shows quasi-spherical formations with dark aureoles on the surface of Si:Sn film. The numbers indicate the sites of Raman micro spectra probing. (b) Raman spectra taken from the three different sites of the sample shown in the panel (a).

crystallization in the “layer exchange” model proceeds through protrusion of Si nanocrystalline formations inside the Sn film.<sup>20</sup>

The layer exchange mechanism could not be applied directly to our results simply because the films in our studies were deposited as a uniform mixture of Si and Sn atoms. Moreover, the formation of dendrite-shaped polycrystalline structures around Sn droplets and existence of a gradient of the partial volume  $X_c$  extending from the Sn droplet towards a periphery of the surrounding dendrite aureole requires alternative explanations. The nucleation of crystals as treated within the layer exchange mechanism<sup>20</sup> assumes diffusion-controlled reactions invoking the thermodynamics of fluctuations to surpass the free-energy barrier. Further crystal growth is facilitated by crystallization heat release to the neighboring regions. For the samples studied in our work, such processes would produce most likely symmetric, oval, or even circular-shaped polycrystalline formations. The protrusions of crystalline Si would be observed towards the interface with the Sn metallic droplets and the expected  $X_c$  gradient would be pointing from the periphery of the aureole toward the interface with the Sn droplet. However, one could hardly find a single symmetric-shaped aureole structure in our samples (see, e.g., Figure 5). Moreover, all the crystalline protrusions in our experiments propagated from the inside of aureoles towards the  $\alpha$ -Si matrix outside the aureoles. Therefore, different crystallization mechanism should be proposed to explain our results.

Following deposition of Si:Sn films at the temperature above the Sn melting point (231.9 °C), Sn atoms may coagulate forming the clusters of liquid Sn (droplet).<sup>2,5</sup> Si atoms diffuse promptly into the formed droplets, creating the molten Si:Sn layer, which could be considered as a solution of silicon in tin. Amorphous Si continues dissolving in this phase until saturation is reached, followed by a rapid supersaturation and local decrease in temperature caused by dissolution of amorphous Si. Formation of the super-saturated

molten Si:Sn layer triggers Si crystallization through either a nucleation process or spinodal decomposition effects.<sup>28–31</sup> In the latter case, within the spinodal region, the homogeneous saturated solution Si:Sn is unstable against fluctuations in density or composition, and there is no thermodynamic barrier to the growth of a new phase, it is purely diffusion-controlled. The shape of a newly formed phase component is essentially irregular as Si crystallization occurs simultaneously along the most favorable paths. Our results did not allow for explicit distinguishing between the two mechanisms (nucleation vs. spinodal decomposition) of a new phase formation. This should not look surprising since in accord with recent studies the scenario of the initial stages of nucleation-growth processes in the two-component system resembles widely the picture of spinodal decomposition.<sup>32</sup> In addition, the basic mechanism of nucleation—surpass of a potential barrier in the evolution to the newly evolving phase—was shown to retain its importance for unstable initial states near the spinodal curve as well.

Si crystallization within the molten Si:Sn layer activates two other processes tending to return the system into the pre-saturated state. The first is Sn atoms segregation on the surface of formed Si nanocrystals. Since the solubility of Sn in crystalline Si is very low ( $\sim 5 \times 10^{19} \text{ cm}^{-3}$ ),<sup>28,33</sup> the excess Sn atoms return back into the molten Si:Sn layer facilitating its under-saturation. The second process is the crystallization heat release that increases the temperature of the adjacent molten Si:Sn layer pushing it below the saturation threshold. Both these processes stimulate further dissolving of amorphous Si. The overall cycle repeats again, creating dendritic, irregular-shaped formations of polycrystalline Si. Similar effects of the dendritic-shaped crystallization inside a thin molten layer of Si:Sn ahead of the advancing crystallization front were briefly reported previously.<sup>5</sup> In our model, the size of formed Si nanocrystals is limited by the thickness of the saturated molten Si:Sn layer. With accumulation of nanocrystals around the Sn droplet, the molten Si:Sn layer is pushed away from the droplet. Assuming that the additional supply of Sn atoms from the droplet is limited by Sn diffusion, the thickness of the saturated molten Si:Sn layer decreases with propagation of the crystallization front away from the droplet. As a result, the average size of formed nanocrystals decreases towards the aureole periphery, which agrees with our observations (see Table III).

The width of the polycrystalline areas (aureoles) around the Sn droplets did not depend on the droplet size. This

TABLE III. The crystal average (dominant) size  $L$  and crystalline phase partial volume  $X_c$  for the probing sites of the film shown in Figure 6(a).

Probing site	$I_c$	$I_a$	$I_c/I_a$	$L$	$X_c$
1	23.7	5.8	4.09	$4.5 \pm 0.2$	$0.8 \pm 0.01$
2	59.8	40.21	1.49	$2.7 \pm 0.1$	$0.6 \pm 0.01$
3	28.8	71.2	0.40	$2.3 \pm 0.1$	$0.28 \pm 0.02$

observation is well understood within the idea of a diffusion-limited supply of Sn atoms from the droplet to the molten Si:Sn layer. While supplying Sn atoms to the crystallization front, the droplet gradually dissolves. Some droplets with very small initial size could be dissolved completely during formation of the poly crystalline phase (see, e.g., Figure 5(d)). It is also reasonable to suggest that a portion of Sn atoms remains between the Si grains (nanocrystals) of the poly crystalline phase, giving rise to a twice-higher Sn content inside the polycrystalline aureoles as compared to the  $\alpha$ -Si matrix as shown with the data of Table II.

The size of formed nanocrystals depends on the temperature, which is well understood within any diffusion-controlled reaction model. Recent studies have demonstrated a monotonous increase in the dominant size of Si nanocrystals with the anneal temperature increase.<sup>21</sup> Those studies suggested that for the anneal temperature of 200–300 °C, the dominant size of the nanocrystals would be within the range of 2.3–4.5 nm. The results of our studies agree fully with the above estimates (see Tables I and III).

In our experiments, the crystallization did not occur in the films containing less than  $\sim 2.5$  at. % of Sn. Similar results were reported previously,<sup>34</sup> showing that an amorphous to polycrystalline phase transformation occurs during annealing of Sn-implanted Si when the peak Sn concentration exceeds about 2 at. %. Apparently, the concentrations of Sn below  $\sim 2$  at. % does not favor coagulation of Sn into droplets and molten Si:Sn layer formation within those Sn droplets. This agrees with the other studies suggesting that the crystallization process of amorphous Si is enhanced by the formation of the liquid Sn phase.<sup>2,5,20</sup>

## V. CONCLUSIONS

The results of this work showed the possibility to fabricate thin films of nanocrystalline Si from a uniformly dispersed Si:Sn alloys at relatively low temperatures. The method of sample preparation used in this work allows a volume manufacturing of nanocrystalline Si films (see also a preliminary account of the results<sup>23</sup>). The most important conclusions of this work are the following: (1) Doping with Sn allows reducing the  $\alpha$ -Si crystallization temperature to below 300 °C and decreasing the dominant size of nanocrystallites to  $\sim 2$  nm. (2) Sn stimulates  $\alpha$ -Si crystallization in a threshold-type manner above the concentrations of approximately 2 at. %. (3) Formation of metallic Sn droplets is a prerequisite for crystallization of  $\alpha$ -Si. Crystallization propagates in the form of dendritic formations from the droplet/ $\alpha$ -Si interface towards the bulk of the  $\alpha$ -Si matrix. (4) Sn-induced crystallization of  $\alpha$ -Si could be explained by formation of a molten Si:Sn (eutectic) layer at the droplet/ $\alpha$ -Si

matrix interface with a spontaneous nucleation and spinodal decomposition within this molten Si:Sn layer.

- <sup>1</sup>M. A. Green, K. Emery, Y. Hishikawa, and W. Warta, *Prog. Photovoltaics* **19**, 84 (2011).
- <sup>2</sup>M. Jeon, C. Jeong, and K. Kamisako, *Mater. Sci. Technol.* **26**(7), 875 (2010).
- <sup>3</sup>O. Nast and A. J. Hartmann, *J. Appl. Phys.* **88**, 716 (2000).
- <sup>4</sup>A. Chandra and B. M. Clemens, *J. Appl. Phys.* **96**, 6776 (2004).
- <sup>5</sup>F. Lin and M. K. Hatalis, in "Beam Solid Interactions: Fundamentals and Applications Symposium" edited by M. Nastasi, L. R. Harriott, N. Herbots, and R. S. Averback (Mater. Res. Soc. Symp. Proc., 1992), Vol. 279, p. 553.
- <sup>6</sup>V. B. Neimash, A. Kraitichinskii, M. Kras'ko, O. Puzenko, C. Claeys, E. Simoen, B. Svensson, and A. Kuznetsov, *J. Electrochem. Soc.* **147**, 2727 (2000).
- <sup>7</sup>V. B. Neimash, A. Kraitichinskii, M. Kras'ko et al., *Ukr. J. Phys.* **45**, 342 (2000).
- <sup>8</sup>C. Claeys, E. Simoen, V. Neimash, A. Kraitichinskii, M. Kras'ko, O. Puzenko, A. Blondeel, and P. Clauws, *J. Electrochem. Soc.* **148**, G738 (2001).
- <sup>9</sup>E. Simoen, C. Claeys, V. B. Neimash, A. Kraitichinskii, N. Krasko, O. Puzenko, A. Blondeel, and P. Clauws, *Appl. Phys. Lett.* **76**, 2838 (2000).
- <sup>10</sup>E. Simoen, C. Claeys, A. M. Kraitichinskii, M. M. Kras'ko, V. B. Neimash, and L. I. Shpinar, *Solid State Phenom.* **82–84**, 425 (2002).
- <sup>11</sup>M. L. David, E. Simoen, C. Claeys, V. Neimash, M. Kras'ko, A. Kraitichinskii, V. Voytovych, A. Kabaldin, and J. F. Barbot, *J. Phys.: Condens. Matter.* **17**, S2255 (2005).
- <sup>12</sup>D. Girginoudi, N. Georgoulas, and F. J. Thanailakis, *J. Appl. Phys.* **66**, 354 (1989).
- <sup>13</sup>A. Mohamedi, M. L. Thye, M. Vergnat, G. Marchal, and M. Piecuch, *Phys. Rev. B* **39**, 3711, (1989).
- <sup>14</sup>G. N. Parsons, J. W. Cook, G. Lucovsky, S. Y. Lin, and M. J. Mantini, *J. Vac. Sci. Technol. A* **4**, 470 (1986).
- <sup>15</sup>R. Ragan, K. S. Min, and H. A. Atwater, *Mater. Sci. Eng., B* **87**, 204 (2001).
- <sup>16</sup>K. A. Johnson and N. W. Ashcroft, *Phys. Rev. B* **54**, 14480 (1996).
- <sup>17</sup>M. Vergnat, M. Piecuch, G. Marchal, and M. Gerl, *Philos. Mag. B* **51**, 327 (1985).
- <sup>18</sup>S. Yu. Shiryayev, J. L. Hansen, P. Kringhyj, and A. N. Larsen, *Appl. Phys. Lett.* **67**, 2287 (1995).
- <sup>19</sup>R. W. Olesinski and G. J. Abbaschian, *Bull. Alloy Phase Diagrams* **5**, 273 (1984).
- <sup>20</sup>A. Mohiddon and G. Krishna, "Metal induced crystallization," in *Crystallization-Science and Technology*, edited by M. R. B. Andreetta (InTech, 2012), pp. 461–480.
- <sup>21</sup>Md. A. Mohiddon and M. G. Krishna, *J. Mater. Sci.* **47**, 6972 (2012).
- <sup>22</sup>V. V. Voitovych, V. B. Neimash, N. N. Krasko, A. G. Kolosiuk, V. Yu. Povarchuk, R. M. Rudenko, V. A. Makara, R. V. Petrunya, V. O. Yuhimchuk, and V. V. Strelchuk, *Semiconductors* **45**, 1281 (2011).
- <sup>23</sup>V. B. Neimash, V. M. Poroshin, O. M. Kabaldin, P. E. Shepelyaviy, V. O. Yuhimchuk, V. A. Makara, and S. U. Larkin, *Ukr. J. Phys.* **58**, 865 (2013).
- <sup>24</sup>E. Bustarret, M. A. Hachicha, and M. Brunel, *Appl. Phys. Lett.* **52**, 1675 (1988).
- <sup>25</sup>H. Richter, Z. P. Wang, and L. Ley, *Solid State Commun.* **39**, 625 (1981).
- <sup>26</sup>H. Campbell and P. M. Fauchet, *Solid State Commun.* **58**, 739 (1986).
- <sup>27</sup>A. Hiraki, *J. Electrochem. Soc.* **127**, 2662 (1980).
- <sup>28</sup>M. Hillert, *Acta Metall.* **9**, 525 (1961).
- <sup>29</sup>G. Horvay and J. W. Cahn, *Acta Metall.* **9**, 695 (1961).
- <sup>30</sup>J. W. Cahn, *J. Chem. Phys.* **42**, 93 (1965).
- <sup>31</sup>L. R. Gomez and D. A. Vega, *Phys. Rev. E* **83**, 021501 (2011).
- <sup>32</sup>J. Schmelzer, A. Abyzov, and J. Moller, *J. Chem. Phys.* **121**, 6900 (2004).
- <sup>33</sup>A. G. Milnes, *Deep Impurities in Semiconductors* (Wiley, New York, 1973), p. 526.
- <sup>34</sup>R. P. Thornton, R. G. Elliman, and J. S. Williams, *J. Mater. Res.* **5**, 1003 (1990).